

# Multimodal optical imaging and spectroscopy for the intraoperative mapping of nonmelanoma skin cancer

Elena Salomatina,<sup>1,2</sup> Alona Muzikansky,<sup>2</sup> Victor Neel,<sup>2,3</sup> and Anna N. Yaroslavsky<sup>1,2,3,a)</sup>

<sup>1</sup>Wellman Center for Photomedicine, Boston, Massachusetts 02114, USA

<sup>2</sup>Massachusetts General Hospital, Boston, Massachusetts 02114, USA

<sup>3</sup>Harvard Medical School, Boston, Massachusetts 02114, USA

(Received 21 April 2008; accepted 15 August 2008; published online 19 May 2009)

Basal cell carcinoma (BCC) is the most common human malignancy, and its incidence increases yearly. In this contribution we investigate the feasibility of combining multimodal reflectance and fluorescence polarization imaging (RFPI) with spectroscopic analysis of the reflectance images for facilitating intraoperative delineation of BCCs. Twenty fresh thick BCC specimens were obtained within 1 h after Mohs micrographic surgeries. The samples were soaked for up to 2 min in an aqueous 0.2 mg/ml solution of methylene blue, briefly rinsed in saline solution, and imaged. Reflectance images were acquired in the range from 395 to 735 nm, with steps of 10 nm. Fluorescence polarization images were excited at 630 nm and registered in the range between 660 and 750 nm. The results yielded by RFPI were qualitatively compared to each other and to histopathology. From the copolarized reflectance images the spectral responses including the optical densities and their wavelength derivatives were calculated. The differences in the spectral responses of the benign and malignant stained skin structures were assessed. Statistical analysis, i.e., Student's t-test, was employed to verify the significance of the discovered differences. Both reflectance and fluorescence polarization images correlated well with histopathology in all the cases. Reflectance polarization images provided more detailed information on skin morphology, with the appearance of skin structures resembling that of histopathology. Fluorescence polarization images exhibited higher contrast of cancerous tissue as compared to reflectance imaging. The analysis of the optical densities and their wavelength derivatives for tumor and normal tissues has confirmed statistical significance of the differences that can be used for intraoperative cancer delineation. The results of the study indicate that spectral analysis is a useful adjunct to RFPI for facilitating skin cancer delineation.

© 2009 American Institute of Physics. [DOI: 10.1063/1.3115646]

## I. INTRODUCTION

Nonmelanoma skin cancers are more common than all other types of human cancers.<sup>1</sup> Basal cell carcinomas (BCCs) constitute 80% of all nonmelanoma skin cancers, and their incidence has been increasing at a dramatic rate. Statistically, every fourth Caucasian will develop at least one lesion during their lifetime. BCCs are disfiguring but rarely fatal (~3000 deaths a year). However, due to their prevalence, the cost of their treatment exceeds \$600 million a year.

Most of BCCs are treated by surgery. As these tumors often occur on the face and rarely metastasize, it is important to preserve as much healthy tissue as possible. However, in many cases, the contrast of the lesions is poor, which complicates visual tumor localization and precise excision. Mohs micrographic surgery<sup>2</sup> is a clinical technique that allows complete control of excision margins during the operation. Mohs surgery<sup>2</sup> has a success rate of 95%,<sup>3</sup> but is used in a minority of cases, as it is expensive, tedious, and time consuming. Thus it is imperative that new techniques and treatment protocols be set in place to address the problem of intraoperative margin control.

Recent advances in optical imaging have made intraoperative, accurate, real-time, and cost-effective inspection of the entire cancer margin technically feasible.<sup>4-9</sup> Several complementary techniques, including dye enhanced reflectance and fluorescence polarization imaging (RFPI), have proven capable of providing real-time high contrast images of skin cancer with a success rate of up to 94%.<sup>4,7</sup> The Food and Drug Administration (FDA)-approved dyes suitable for *in vivo* use, such as methylene blue (MB), are applied to the lesions, as the intrinsic differences in optical signals from normal and diseased tissues are often subtle.<sup>10</sup> MB has been successfully applied to grossly demarcate neoplastic tumors in the bladder,<sup>11-13</sup> tumors of the pancreas,<sup>14</sup> and Barrett's esophagus metaplasia.<sup>15,16</sup> Even though it has been reported that MB accumulates to a much greater extent in the mitochondria of cancerous cells as compared to normal cells,<sup>17</sup> it is not 100% specific. Several healthy structures, such as hair follicles, sebaceous glands, and epidermis retain some dye. However, the appearance of these tissues and the concentration of the dye differ considerably from those of cancer. Thus the results provided by RFPI may be further improved by incorporating spectral analysis, assuming that practical time-efficient algorithms can be developed that would allow real-time tumor delineation process.

<sup>a)</sup> Author to whom correspondence should be addressed. Electronic mail: yaroslav@helix.mgh.harvard.edu. Tel.: 617-726-1590. FAX: 617-726-8566.

TABLE I. Study subjects.

No.	Age	Gender	Type of the lesion	Site	$L \times W \times H$ (cm)
1	84	M	Nodular BCC	Right temple	$1.8 \times 0.8 \times 0.25$
2	64	M	Nodular BCC	Left temple	$1.5 \times 0.7 \times 0.21$
3	73	M	Nodular BCC	Left neck	$1.4 \times 0.7 \times 0.21$
4	75	M	Nodular BCC	Left helix	$2.1 \times 0.8 \times 0.25$
5	74	F	Nodular BCC	Left nasal tip	$2.8 \times 1.0 \times 0.27$
6	64	F	Micronodular BCC	Right middle eyebrow	$1.0 \times 0.4 \times 0.18$
7	58	F	Nodular BCC	Middle nasal bridge	$1.3 \times 0.6 \times 0.20$
8	87	F	Nodular BCC	Left nose	$1.9 \times 0.9 \times 0.23$
9	67	M	Nodular BCC	Left nasal tip	$1.3 \times 0.9 \times 0.21$
10	59	M	Superficial and nodular BCC	Left scalp	$2.0 \times 1.7 \times 0.24$
11	60	M	Nodular BCC	Left upper forehead	$0.7 \times 0.3 \times 0.12$
12	48	M	Nodular BCC	Right nasal wing	$0.9 \times 0.3 \times 0.12$
13	83	M	Superficial and nodular BCC	Left temple	$2.4 \times 1.0 \times 0.23$
14	58	M	Nodular BCC	Left nasal sidewall	$1.0 \times 0.5 \times 0.19$
15	52	F	Nodular BCC	Right upper lip	$1.7 \times 0.7 \times 0.20$
16	76	F	Nodular BCC	Left middle nasal bridge	$1.5 \times 0.8 \times 0.20$
17	70	F	Nodular BCC	Left temple	$2.5 \times 1.1 \times 0.27$
18	64	M	Nodular BCC	Left upper neck	$2.2 \times 1.2 \times 0.25$
19	66	M	Nodular BCC	Right nasal bridge	$1.7 \times 0.8 \times 0.22$
20	78	M	Nodular BCC	Middle scalp	$1.4 \times 0.6 \times 0.21$

## II. MATERIALS AND METHODS

### A. Tissue preparation and handling

Twenty (20) freshly excised thick skin specimens with residual nonmelanoma skin cancers were obtained from 20 patients under an protocol approved by the Institutional Review Board from Mohs micrographic surgeries<sup>2</sup> performed at the Dermatologic Surgery Unit of Massachusetts General Hospital. The information on the lesions is summarized in Table I.

In our study we used commercially available MB (MB injection, 1%, American Regent Inc., Shirley, NY). The MB was diluted to a concentration of 0.2 mg/ml using Dulbecco's phosphate-buffered solution (1X, pH 7.4, Mediatech, Herndon, VA) and kept at 37 °C. The specimens were soaked in diluted MB for up to 2 min. To remove excess of the dye, the specimens were briefly rinsed in saline solution, pH 7.4. Then the tissue was placed dermal side up into Petri dish on gauze moistened with saline solution, covered with a microscopic slide, and imaged. All the experiments were performed at room temperature.

### B. Polarization enhanced reflectance and fluorescence imaging system

The imaging setup is presented in Fig. 1. We used a 500 W Xe-arc lamp (Spectra Physics Oriel, Stratford, CT) coupled with an MS 275 grating monochromator (Oriel Instruments, Stratford, CT) as a light source. The light was delivered to the tissue via the light guide (Oriel Instruments, Stratford, CT). A holographic diffuser (15°, Edmund Optics, Barrington, NJ) and a linearly polarizing filter (Meadowlark Optics, Frederick, CO) were introduced into the path of the incident light to provide a homogeneous linearly polarized illumination of the specimen. A charge-coupled device

(CCD) CoolSnap HQ camera (Roper Scientific, Tucson, AZ), equipped with an achromatic CCD lens (Linos Photonics Inc., Milford, MA) and a rotating linearly polarizing filter (Meadowlark Optics, Frederick, CO), was used to acquire co- and cross-polarized reflectance images of the specimens. For fluorescence imaging, an additional long-pass filter (660AELP, Omega Optical, Brattleboro, VT) was attached to the camera lens. The angle between the excitation and emission polarizer was approximately 55°. The maximal field of view provided by the system was  $3.3 \times 2.9$  cm<sup>2</sup>, and lateral resolution was better than 25 μm. The axial resolution varied between 70 and 200 μm.<sup>4</sup> The power density of the light on the tissue never exceeded 0.3 mW/cm<sup>2</sup>. Illumination, acquisition, and image processing were controlled via the codes developed using the METAMORPH 6.0R1 imaging software (Molecular Devices Corporation, CA). The reflectance measurements required approximately up to 3 s for both polarizations. The fluorescence imaging required up to 5 s.

### C. Image processing

Superficial reflectance images were calculated as a difference of experimentally acquired co- and cross-polarized images in the range of 395–735 nm with steps of 10 nm.

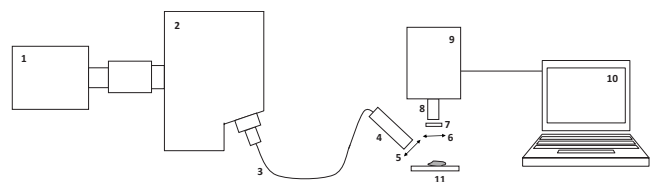


FIG. 1. Experimental setup for RFPI. (1) Xe-arc lamp, (2) monochromator, (3) light guide, (4) illuminator, (5) and (6) linearly polarizing filter, (7) long-pass emission filter, (8) CCD lens, (9) CCD camera, (10) PC, and (11) sample stage with specimen.

Fluorescence polarization images of the tissues were calculated as  $F = (F_{\text{co}} - F_{\text{cross}}) \times 100 / (F_{\text{co}} + F_{\text{cross}})$ , where  $F$  is a fluorescence polarization image, and  $F_{\text{co}}$  and  $F_{\text{cross}}$  are co- and cross-polarized fluorescence emission images, respectively. Image processing was performed in real time.

#### D. Spectral analysis

Copolarized reflectance images were used to determine the values of diffuse reflectance and the optical density for each skin structure in the image at a given wavelength. Stacks of 35 copolarized reflectance light images were acquired in the range from 395 to 735 nm, with steps of 10 nm. A calibrated gray reference (reflectance value  $\sim 35\%$  in the range from 395 to 735 nm) was placed in the camera field of view to enable absolute quantification of diffuse reflectance. Each experimental spectrum was divided by the value of the diffuse reflectance measured at 735 nm. As this wavelength lies outside the absorption band of MB, this normalization allowed for the compensation of possible impact of background absorption and scattering on the spectral analysis. For all copolarized reflectance images acquired at each wavelength, the absolute diffuse reflectance and optical density of the skin structures were calculated using the following expressions:

$$R^\lambda = 0.35R_s^\lambda / R_{\text{ref}}^\lambda,$$

$$\text{OD}^\lambda = \log(1/R^\lambda),$$

where  $R^\lambda$  is the absolute diffuse reflectance of the skin structures at a given wavelength,  $R_{\text{ref}}^\lambda$  is the relative diffuse reflectance of the gray reference at a given wavelength,  $R_s^\lambda$  is the relative diffuse reflectance of the skin structures at a given wavelength, and  $\text{OD}^\lambda$  is the optical density of the skin structures at a given wavelength.

Then the wavelength derivatives of the optical densities were calculated.

#### E. Statistical analysis

A Student's two-tailed t-test (STATISTICA 6.0, StatSoft, Inc., Tulsa, OK) was used to evaluate the significance of the difference in obtained optical densities and their wavelength derivatives between normal skin structures and cancerous tissues for a set of selected wavelengths. The differences in optical densities and their wavelength derivatives between healthy and cancerous tissues were considered to be statistically significant when the calculated probability value ( $p$ -value) was equal or less than 0.05. The results were summarized in a table to outline the spectral regions, where the optical densities and their wavelength derivatives of normal and cancerous tissues differed significantly.

#### F. Comparison to histopathology

En face H&E stained frozen sections were processed from the imaged tissue blocks using standard Mohs methodology.<sup>2</sup> High-resolution images of the sections were obtained using a SPOT RT microscope digital camera (Diagnostic Instruments, Inc., Sterling Heights, MI) coupled with an Axiophot microscope (Carl Zeiss, Thornwood, NY).

The tumor margins in the H&E slides were determined by a certified pathologist, who had no access to the optical images. The quantitative reflectance (at 665 nm) and fluorescence polarization images were compared to histology.

### III. RESULTS AND DISCUSSION

In total, we have imaged and spectroscopically analyzed twenty (20) BCC specimens. The spectral responses, i.e., optical densities and their wavelength derivatives, of the following structures were analyzed and stored in the database: cancer, hair follicles, sebaceous glands, epidermis, collagen, and subcutaneous fat.

Example color-coded quantitative reflectance and fluorescence polarization images of a BCC shown in Figs. 2(a) and 2(b), respectively, are compared to H&E histopathology, shown in Fig. 2(c). The tumor in Fig. 2(c) is outlined with red by a certified pathologist. The location, dimensions, and shape of the tumor correlate well with those in the histopathology [Fig. 2(c)]. It is worth noting that cancer in the optical images [see Figs. 2(a) and 2(b)] exhibits higher contrast in comparison to histopathology at the same magnification [see Fig. 2(c)].

As expected the superficial reflectance image demonstrates that the highest optical density, which is color-coded with red, corresponds to the location of the tumor. However, some parts of the epidermis (shown with solid white and black arrows in optical and histological images, respectively), hair follicles (dotted white and black arrows in optical and histological images, respectively), and sebaceous glands (dashed white and black arrows in optical and histological images, respectively) accumulate considerable amount of dye and can be confused with tumor. Straightforward qualitative comparison with corresponding histopathology [Fig. 2(c)] demonstrates that epidermis, hair follicles, and sebaceous glands may be discriminated from tumor by the morphological appearance. Nonetheless, these structures may be involved with tumor, and therefore a time-efficient method that could reliably detect small cancer nests and is compatible with reflectance polarization imaging would be valuable. In the fluorescence polarization image, presented in Fig. 2(b), tumor exhibits higher fluorescence polarization (color-coded with green) as compared to the normal tissues of the sample. Skin appendages, such as hair follicles and sebaceous glands, cannot be easily distinguished. However, even in fluorescence polarization images, there are several bright pixels along the epidermis (solid white arrow) and in the vicinity of the hair follicles (dotted white arrow) that may manifest malignancy.

Thus, several normal skin structures, such as hair follicles, sebaceous glands, and epidermis, retain some dye. Some of them appear red in color-coded reflectance images and green in color-coded fluorescence images. To resolve this ambiguity we have analyzed the spectral responses of all skin structures present in the reflectance images. Figure 2(d) shows averaged over the sample wavelength dependences of the optical densities of MB-stained cancer sample structures. The MB concentration is the highest in the tumor, which results in the increase in optical density in the spectral range

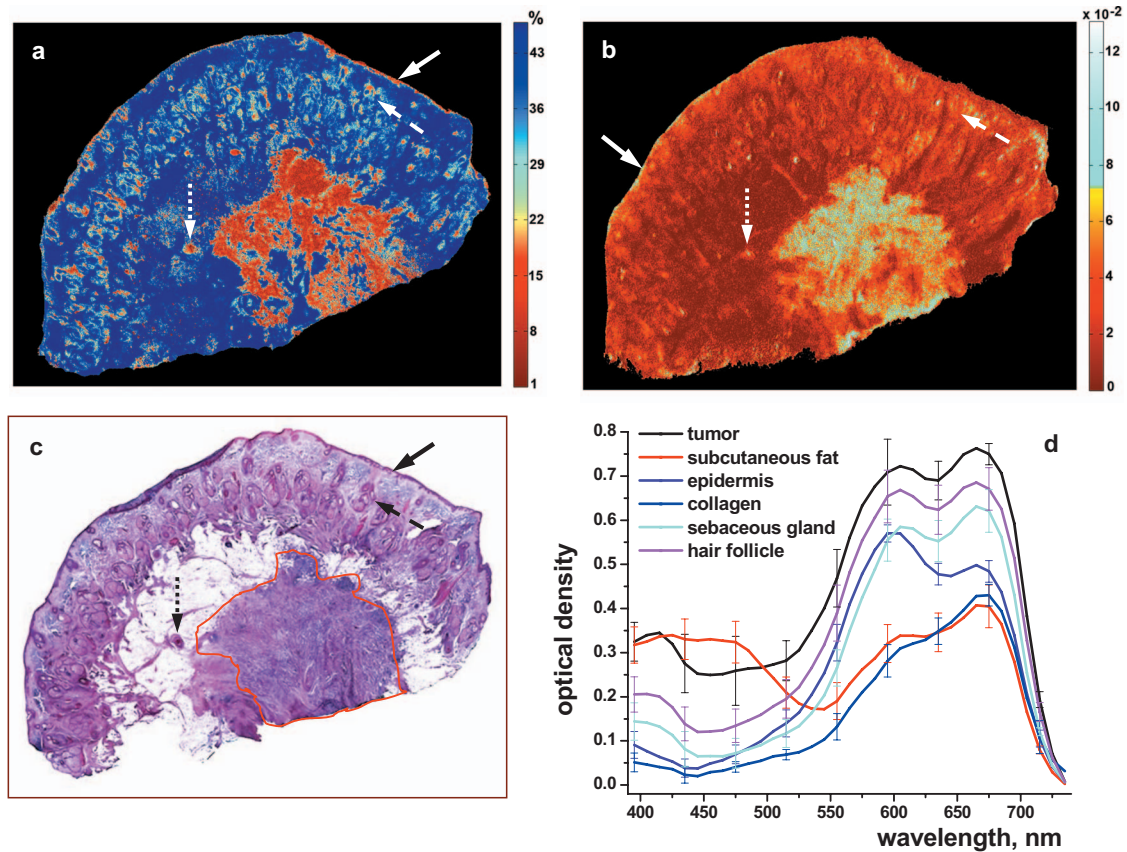


FIG. 2. (Color) Example specimen with BCC (field of view:  $16 \times 7$  mm<sup>2</sup>; site: scalp): (a) color-coded superficial reflectance image at 665 nm (bar, absolute reflectance), (b) fluorescence polarization image excited at 615 nm and registered in the range between 660 and 750 nm (bar, fluorescence polarization), (c) corresponding H&E frozen histology with the tumor borders (red line) outlined by certified pathologist, and (d) averaged optical density spectra of cancer and normal structures (bars, standard deviation). In the images the solid arrow points to the epidermis, the dashed arrow points to the sebaceous gland, and the dotted arrow points to the hair follicle.

that corresponds to the two absorption maxima of MB around 615 and 665 nm. Even though the concentration of the dye is lower in hair follicles, the spectral responses of these two structures are quite similar. The spectral responses of the sebaceous glands demonstrate that the optical density of these skin appendices is much lower in the MB absorption wavelength range between 570 and 710 nm, as compared to cancer. In the spectrum of epidermis, the MB absorption peak at 615 nm is more pronounced than the latter at 665 nm. This feature allows for delineation between cancer and epidermis, as the former exhibits the opposite distribution of absorption peak intensities. In addition, the comparison of the optical density curves of epidermis and cancer shows that the tumor accumulates much more dye and exhibits considerably higher optical density in the vicinity of the 665 nm MB absorption band. Collagen and fat do not accumulate significant amounts of the dye, and therefore can be easily distinguished from the tumor. In addition, subcutaneous fat spectra exhibit higher optical density in the wavelength range from 395 to 560 nm, as compared to other skin structures. This phenomenon can be explained by higher hemoglobin content in subcutaneous fat.<sup>10</sup> It is notable that all skin structures exhibit different spectral responses within the absorption band of MB, due to the different uptake of the dye by skin tissues. To confirm that the spectral signatures of MB-stained skin structures can be reliably used for discrimi-

nating cancer from benign tissue we have determined and statistically analyzed the optical densities of cancer, hair follicles, sebaceous glands, epidermis, collagen, and fat collected from 20 fresh thick samples containing BCCs. The averaged dependences of the optical densities on the wavelength for all the skin structures that were investigated are shown in Fig. 3. The optical density of cancerous tissue was substantially higher as compared to other skin tissues within the absorption bands of MB. In addition, the differences in the optical densities of epidermis and cancer were considerable in the wavelength range between 390 and 485 nm [see Fig. 3(c)]. This spectral range corresponds to the Soret absorption band of hemoglobin. It is known that cancerous tissue always contains blood. In contrast, healthy epidermis is bloodless. Therefore, the observed differences may be explained by the difference in blood content of the tumor and the epidermis. Due to variations in hemoglobin content and to the low dye uptake by collagen and fat, the differences in the optical densities of collagen-tumor and fat-tumor pairs were substantial in the entire spectral range investigated. Differences in blood content between cancer and adjacent normal skin are highly variable. In addition, reflectance measurements may be affected by oxygenation of blood as well as by location of the lesion on the body. Thus, the identified differences in the spectral range of hemoglobin absorption cannot provide a reliable basis for tissue discrimination.

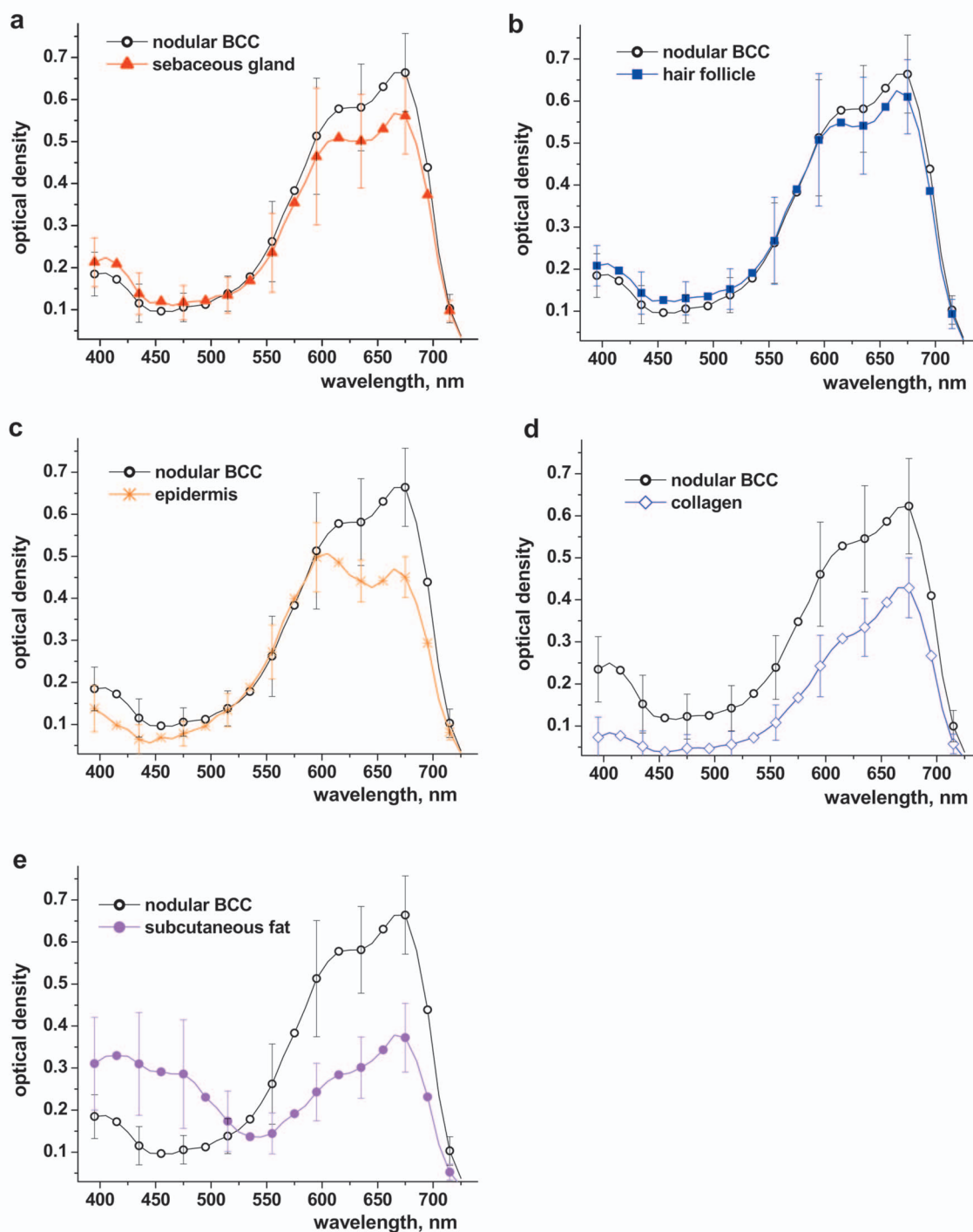


FIG. 3. (Color) Optical density spectra of cancer-healthy structure pairs, averaged over 20 samples; bars are standard deviations. (a) BCC and sebaceous gland, (b) BCC and hair follicle, (c) BCC and epidermis, (d) BCC and collagen, and (e) BCC and subcutaneous fat.

Comparative analysis revealed, that for all the structures investigated, with the possible exception of hair follicles [Fig. 3(b)], the differences in the spectral range from 615 and 700 nm between cancerous and healthy skin structures were obvious [see Figs. 3(a) and 3(c)–3(e)]. Therefore, we have decided to focus our further analysis on the spectral range between 600 and 735 nm.

To address the problem of reliable spectroscopic discrimination of the tumor and the hair follicles we have calculated and analyzed the differences in the wavelength derivatives of the optical densities for cancer-normal tissue

pairs. It has been published that MB displays different absorptive properties depending on the biochemical environment.<sup>18,19</sup> Thus, we hypothesized that the observed subtle deviations in the slopes of the MB-stained cancer and hair follicle optical density curves may be caused by differences in the biochemical environment of these two structures. Therefore, if these deviations are reproducible, they may be used for the reliable differentiation of cancer. The resulting dependences of the wavelength derivatives of the optical densities are presented in Fig. 4.

To evaluate the significance of the differences between

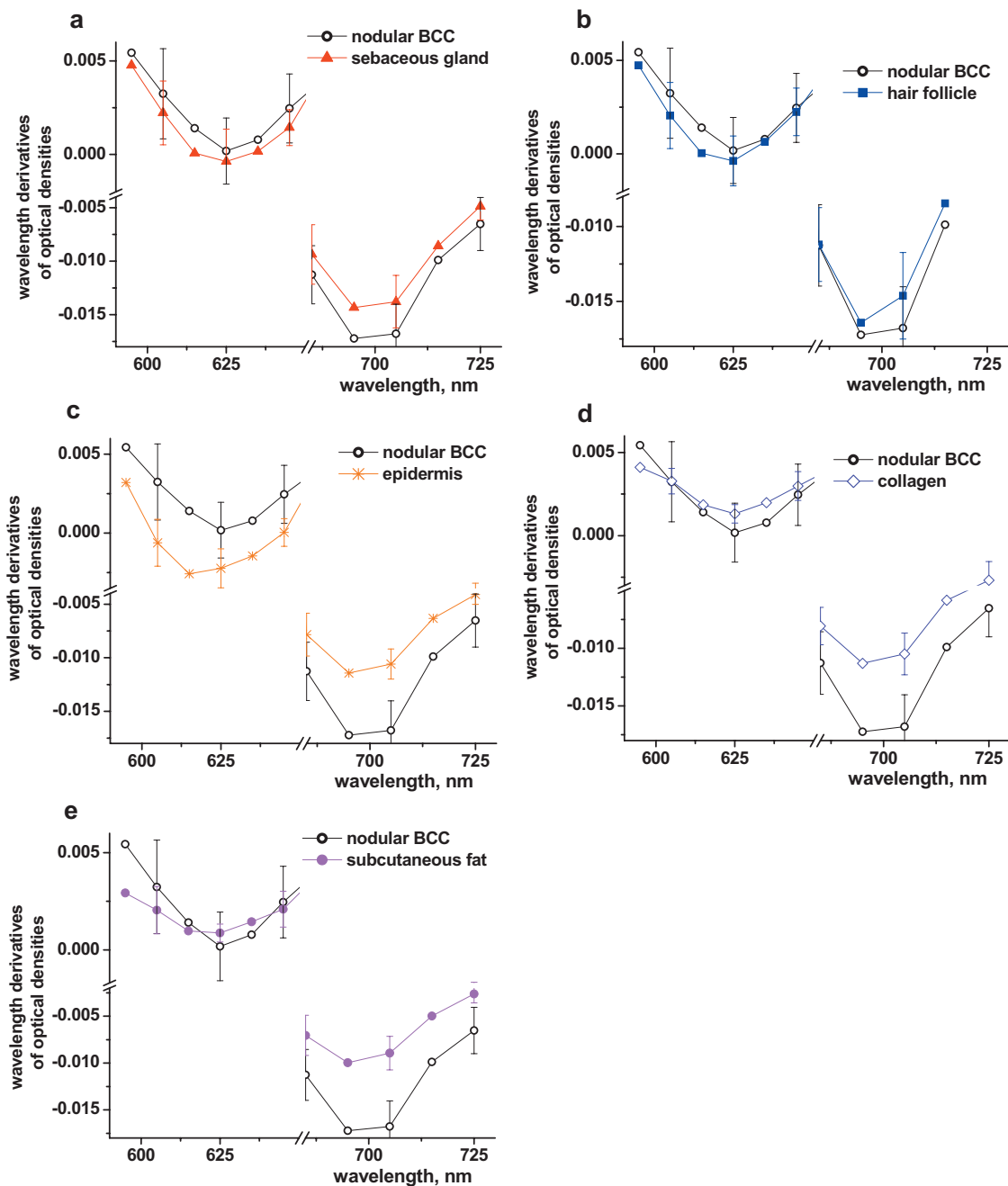


FIG. 4. (Color) The spectra of the optical density wavelength derivatives, averaged over 20 samples; bars are standard deviations. (a) BCC and sebaceous gland, (b) BCC and hair follicle, (c) BCC and epidermis, (d) BCC and collagen, and (e) BCC and subcutaneous fat.

optical densities and their wavelength derivatives of normal and cancer tissue pairs we have used unpaired two-tailed t-tests. The choice to perform pairwise t-test rather than starting with standard analysis of variance (ANOVA) hinges upon our intention to identify regions of difference between the cancer tissue and other normal skin type tissues. To that end we chose to test the independent normal skin type tissue samples against the cancer tissue samples one by one. The results of the tests are summarized in Table II. These results demonstrate that for all cancer-normal tissue pairs, with the exception of the hair follicles, there exist statistically significant differences in the optical densities at the wavelength of 665 nm, which corresponds to one of the absorption maxima of MB. The statistically significant differences in the wave-

length derivatives of the optical densities between cancer and hair follicles were found at the wavelengths of 615, 705, and 735 nm, out of which 615 nm corresponds to another absorption maximum of MB. Interestingly, for all the cancer-normal tissue pairs, the differences in the wavelength derivatives of the optical densities were significant at 705 nm. Thus, we were able to identify the spectral ranges suitable for the reliable differentiation of the cancerous and normal skin using spectral analysis of the reflectance images. Importantly, these wavelength ranges include the 615 and 665 nm, which correspond to the absorption maxima of MB, which means that the spectral analysis of the images can be incorporated into the tumor detection process without altering the imaging procedure or adding complexity and time. Even

TABLE II. Spectral regions of maximal optical contrast between cancer and normal skin structures as determined by unpaired two-tailed t-test at the significance level of 0.05.

Tumor versus healthy structure pairs	Optical density		Derivatives	
	Wavelength range of statistically significant difference (nm)	<i>p</i> -values	Wavelength range of statistically significant difference (nm)	<i>p</i> -values
Collagen	[595; 725]	$0 \leq p \leq 0.00045$	595	$p = 0.0114$
			625	$p = 0.0095$
			635	$p = 0.0021$
			[675; 725]	$0 \leq p \leq 0.036$
Epidermis	[615; 715]	$0 \leq p \leq 0.019$	[595; 665]	$0 \leq p \leq 0.0017$
			[685; 725]	$0 \leq p \leq 0.000001$
Subcutaneous fat	[595; 725]	$0 \leq p \leq 0.000001$	595	$p = 0.000031$
			[675; 725]	$0 \leq p \leq 0.017$
Hair follicle	...	...	615	$p = 0.035$
			705	$p = 0.021$
			725	$p = 0.009$
Sebaceous gland	[625; 695]	$0.001 \leq p \leq 0.032$	645	$p = 0.034$
			[685; 705]	$0.0008 \leq p \leq 0.035$
			725	$p = 0.011$

though in general it might seem that complete spectroscopic analysis of every pixel in the image for the entire visible spectral range would be an appropriate approach, in practice it is not the most optimal way of handling the problem. First, analysis of even ten (10) wavelengths for the  $1100 \times 1300$  pixels will require prohibitively long time, rendering the method unsuitable for the intraoperative use. Second, it will be redundant, as the reflectance and fluorescence polarization images provide sufficiently accurate information for the majority of pixels. Thus, the combination of the RFPI with the two wavelength spectral analysis of several pixels, which appear suspicious to a surgeon who inspects the images intraoperatively, seems like a more practical approach, suitable for use in clinical practice.

To summarize, the results of our study confirm that analysis of the optical densities and their wavelength derivatives may facilitate nonmelanoma skin cancer delineation using RFPI. The database of the tissue spectral responses collected in this study and the results of the statistical analysis indicate that the spectral range corresponding to the absorption bands of MB can be used for reliable differentiation of cancer. Our tumor demarcation technique requires imaging at multiple wavelengths. However, since the optical densities and their wavelength derivatives of all the normal skin structures investigated are significantly different from those of cancer at 615 and 665 nm, quick spectroscopic analysis at only two (2) interrogation wavelengths should be sufficient. The data presented above indicate that RFPI combined with spectral analysis may become a real-time powerful tool for the accurate intraoperative cancer delineation.

## ACKNOWLEDGMENTS

Help with the histopathological analysis provided by Dr. Munir Al-Arashi is gratefully acknowledged. This study was

funded by the National Institutes of Health (Grant No. R01 EB002423-01).

- <sup>1</sup>E. Dahl, M. Aberg, and E. L. Rausing, *Cancer* **70**, 104 (1992).
- <sup>2</sup>F. E. Mohs, *Arch. Surg. (Chicago)* **42**, 279 (1941).
- <sup>3</sup>P. Casson, *Clin. Plast. Surg.* **7**, 301 (1980).
- <sup>4</sup>A. N. Yaroslavsky, V. Neel, and R. R. Anderson, *J. Invest. Dermatol.* **121**, 259 (2003).
- <sup>5</sup>V. Q. Chung, P. J. Dwyer, K. S. Nehal, M. Rajadhyaksha, G. M. Menaker, C. Charles, and S. B. Jiang, *Dermatol. Surg.* **30**, 1470 (2004).
- <sup>6</sup>J. Strasswimmer, M. C. Pierce, B. H. Park, V. Neel, and J. F. de Boer, *J. Biomed. Opt.* **9**, 292 (2004).
- <sup>7</sup>A. N. Yaroslavsky, V. Neel, and R. R. Anderson, *Opt. Lett.* **29**, 2010 (2004).
- <sup>8</sup>A. N. Yaroslavsky, J. Barbosa, V. Neel, Ch. DiMarzio, and R. R. Anderson, *J. Biomed. Opt.* **10**, 014011 (2005).
- <sup>9</sup>A. N. Yaroslavsky, E. Salomatina, V. Neel, R. R. Anderson, and T. J. Flotte, *J. Biomed. Opt.* **12**, 014005 (2007).
- <sup>10</sup>E. Salomatina, B. Jiang, J. Novak, and A. N. Yaroslavsky, *J. Biomed. Opt.* **11**, 064026 (2006).
- <sup>11</sup>W. B. Gill, J. L. Huffman, E. S. Lyon, D. H. Bagley, H. W. Schoenberg, and F. H. Straus, *Cancer* **53**, 2724 (1984).
- <sup>12</sup>A. V. Kaisary, *Urology* **28**, 100 (1986).
- <sup>13</sup>I. Fukui, M. Yokokawa, G. Mitani, F. Ohwada, M. Wakui, M. Washizuka, T. Tohma, K. Igarashi, and T. Yamada, *J. Urol.* **130**, 252 (1983).
- <sup>14</sup>I. J. Fedorak, T. C. Ko, D. Gordon, M. Flisak, and R. A. Prinz, *Surgery* **113**, 242 (1993).
- <sup>15</sup>M. I. Canto, S. Setrakian, R. E. Petras, E. Blades, A. Chak, and M. V. Sivak, Jr., *Gastrointest. Endosc.* **44**, 1 (1996).
- <sup>16</sup>G. M. Eisen, E. A. Montgomery, N. Azumi, D. P. Hartmann, P. Bhargava, M. Lippman, and S. B. Benjamin, *Gastrointest. Endosc.* **50**, 814 (1999).
- <sup>17</sup>A. R. Oseroff, D. Oshooha, G. Ara, D. McAuliffe, J. Foley, and L. Cincotta, *Proc. Natl. Acad. Sci. U.S.A.* **83**, 9729 (1986).
- <sup>18</sup>D. Severino, H. C. Junqueira, M. Gugliotti, D. S. Gabrielli, and M. S. Baptista, *Photochem. Photobiol.* **77**, 459 (2003).
- <sup>19</sup>A. Czimerová, L. Jankovic, and J. Bujdák, *J. Colloid Interface Sci.* **274**, 126 (2004).